RESEARCH ARTICLE | SEPTEMBER 09 2025

Upscale rarefied volatile diffusion in porous media: A pore network modeling approach *⊙*

Sunpeng Zhou 💿 ; Ke Xu 🔀 💿



Physics of Fluids 37, 096608 (2025) https://doi.org/10.1063/5.0284757





Articles You May Be Interested In

Spectral condensation and bidirectional energy transfer in quasi-geostrophic turbulence above small-scale topography

Physics of Fluids (August 2024)

Anomalous transport in a porous medium with randomly packed ellipse cavities

Physics of Fluids (December 2022)

Hydrodynamic dispersion in thin channels with micro-structured porous walls

Physics of Fluids (July 2018)





Upscale rarefied volatile diffusion in porous media: A pore network modeling approach

Cite as: Phys. Fluids **37**, 096608 (2025); doi: 10.1063/5.0284757 Submitted: 10 June 2025 · Accepted: 18 August 2025 · Published Online: 9 September 2025









Sunpeng Zhou¹ (D) and Ke Xu^{1,2,a)} (D)



AFFILIATIONS

- ¹Peking University School of Mechanics and Engineering Science, Department of Energy and Resources Engineering, Beijing 100871, China
- ²Peking University Research Institute of Extraterrestrial Material, Beijing 100871, China

ABSTRACT

On airless bodies such as the Moon and cometary nuclei, volatiles redistribute and escape through the surface porous regolith layer. Under a highly vacuum environment, volatiles migrate through porous media via Knudsen diffusion, where volatile molecules rarely collide with each other and instead jump directly from one solid surface to another. Although Knudsen diffusion in microscopic confinement can be numerically resolved by Monte Carlo-based methods, studying its upscaled behavior at the representative elementary volume scale remains challenging due to the high computational cost and inherent geometric and kinetic randomness. In this paper, we develop a probabilitybased pore network modeling (p-PNM) approach to model upscaled Knudsen diffusion behaviors in porous media. This approach is inspired by the duality of the molecular motion trajectories: volatile transport in pore-bodies satisfies the Markov property (the exit probability of molecules is independent of their residence time), while that in pore-throats does not satisfy the Markov property. This p-PNM approach is validated in ball-stick geometries and typical sedimentary geometries, with geometric randomness, surface adsorption energy heterogeneity, and temperature gradients. It enables upscaled modeling of volatile transport through regolith on airless body surfaces, for geoscience research and for in situ recovery of resources on the Moon and other airless bodies.

Published under an exclusive license by AIP Publishing. https://doi.org/10.1063/5.0284757

I. INTRODUCTION

In certain regions of airless bodies, such as the Moon and cometary nuclei, volatile components—such as water, carbon dioxide, and methanol—migrate and redistribute through the surface regolith. The surfaces of comets⁶ or lunar regolith⁷ are composed of loose and weakly-bound particles with high porosity (50%-80%)^{8,9} representing sedimentary structures.⁶ The retention, abundance, distribution, and escape dynamics of volatiles within such sedimentary media are of great geochemical significance, 6,10,11 and are also crucial for in situ recovery of ice deposits. 12-1

Under extremely high vacuum conditions, volatile molecules migrate through intergranular voids in regolith, where pore dimensions are orders of magnitude smaller than the molecular mean free path. This regime is quantified by the Knudsen number (Kn), defined as the ratio of molecular mean free path to characteristic pore size. 16 On the lunar surface, for instance, gas densities $(1 \times 10^4 - 2 \times 10^5)$ molecules/cm³), temperatures (29–400 K), ^{17,18} and regolith grain sizes $(1.40-9.35 \,\mu\text{m}, \text{ covering 95\% of Chang'e-5 samples})^{19}$ yield exceptionally high Kn values $(1 \times 10^{12} \text{ to } 1.8 \times 10^{14})$, effectively approaching infinity. Such conditions correspond to Knudsen diffusion or free molecular flow, ^{20,21} where molecules are interrupted solely by molecule-wall collisions. Unlike nanoscale systems (e.g., shale and catalysts^{22,23}) that also exhibit high Kn, regolith pores are notably larger, typically ranging from 1 to $10\,\mu m$ (comparable to particle size) and potentially up to $100 \,\mu\mathrm{m}$ in some estimations. This large pore size allows molecules to maintain straight-line trajectories between collisions with solid walls, as van der Waals interactions are only effective within a few nanometers.²⁴ Consequently, the Knudsen diffusion coefficient is primarily governed by the geometric configuration of the porous matrix. Knudsen²⁵ proposed the calculation of the Knudsen diffusion coefficient D_{Kn} based on the infinitely long and straight circular tube

$$D_{Kn} = \frac{1}{3}\overline{\nu}d,\tag{1}$$

where d is the tube diameter or characteristic pore size, 26 and \overline{v} is the mean speed of gas molecules. For finite-length channels, the lengthto-diameter ratio becomes important, and the Clausing formula²⁷ can be adopted.

^{a)}Author to whom correspondence should be addressed: kexu1989@pku.edu.cn.

Unlike that in straight tubes, varying geometric confinements largely complicate the modeling of Knudsen diffusion in porous media such as lunar regolith. To correlate the transport phenomena in straight tubes and in porous media, a commonly adopted and intuitive approach is to introduce "tortuosity," defined as the ratio of the actual flow path length to the direct path length.^{28,29} However, this method is not physically valid for Knudsen diffusion because the local Knudsen diffusivity [defined by Eq. (1)] is ill-defined, since the characteristic pore size is unclear. ^{26,30} Russ³¹ calculated Knudsen tortuosity in disordered linear pores by dividing them into analytically tractable subunits. Yet, this approach is limited to specific structures. Alternatively, the Derjaguin formula^{32,33} links the straight-line trajectory length distribution (determined by pore structure) to the diffusion coefficient. However, it relies on molecular trajectory data and cannot directly relate geometry to diffusivity. In addition, for layered structures, diffusion coefficients can be calculated using the transmission probabilities of gas molecules through the layers.³⁴ Despite these efforts, bridging the gap between local porous structures and upscaled Knudsen diffusion in a general and predictive way is still highly challenging.

In this study, we develop a probability-based pore network model (p-PNM) that predicts Knudsen diffusion coefficients directly from pore structure characteristics. We first conduct Monte Carlo numerical experiments of Knudsen diffusion in porous media to investigate local trajectory (Sec. II). We then show the rationality and necessity to establish the p-PNM model for Knudsen diffusion in porous media according to observations in numerical experiments, describe the p-PNM algorithm, theoretically derive key parameters, and verify this framework against numerical experiments (Sec. III). At last, we demonstrate the application of the p-PNM approach in upscaling pore-scale characteristics to the REV scale and provide examples illustrating its capabilities in modeling heterogeneous media and temperature-driven diffusion (Sec. IV).

II. NUMERICAL EXPERIMENTS

A. Algorithm

We adopt the test particle Monte Carlo (TPMC) method for numerical simulation of volatile diffusion in porous media under the infinite *Kn* condition. TPMC is a particle-based stochastic simulation method³⁵ that simplifies molecular simulations by disregarding molecule-molecule collisions and focusing solely on molecule-wall collisions. This method is well-suited for modeling free molecular flow, which inherently corresponds to a large Knudsen number. The versatility of the TPMC method has been demonstrated in diverse applications, including the analysis of space vehicles,³⁶ particle accelerators,³⁷ and fibrous porous media.³⁸

The approach for a porous medium is as follows:

- (1) Compute the signed distance (the shortest distance from any point in space to the solid wall) in the³⁹ field of the porous media. Positive signed distance values correspond to void regions, while negative values correspond to the solid matrix.
- (2) Initialize the coordinates and velocities of all simulated molecules. The molecular velocities follow a Maxwell–Boltzmann distribution at equilibrium, with both direction and magnitude satisfying the statistical distribution [Eqs. (2) and (3)]. For the simulation of molecular self-diffusion, the initial condition is established by placing self-diffusion molecules at the origin with velocities sampled from the Maxwell–Boltzmann distribution.
- (3) Simulate the molecular motion to obtain trajectories. Molecules travel in straight-line segments until they collide with solid walls, adsorb, reflect, and then continue moving in straight lines [see Fig. 1(a)]. We employ the ray tracing method, 40,41 where, at each step, the molecule moves by the signed distance from its current position unless it's close enough to the wall. When the signed distance of the arrival point decreases below a

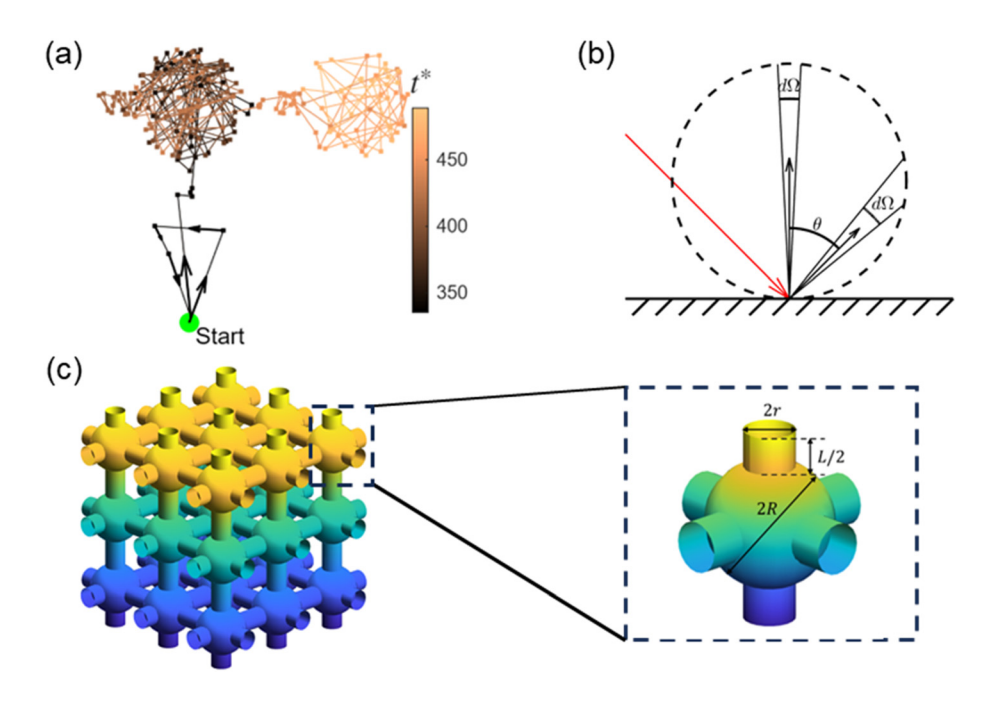


FIG. 1. (a) 2D projection of a simulated molecular trajectory varied with dimensionless time ($t^* = \overline{v}t/R$), consisting of straight-line segments connecting two molecule-wall collision points (dots). (b) Diagram of diffuse reflection. The direction of molecular reflection (black arrow) is independent of the incident direction (red arrow), and the probability of reflection into a solid angle $(d\Omega)$ is proportional to the cosine of the reflection angle (θ) . (c) The periodic 3D structure used in the simulation is the ball-and-stick structure. It consists of spherical pore-bodies connected by cylindrical pore-throats. The centers of the pore-bodies are distributed at the vertices of the cubes. Each periodic unit consists of a pore-body surrounded by six half pore-throats. The geometric parameters include pore-body radius (R), pore-throat radius (r), and pore-throat length (L).

predetermined threshold, adsorption and reflection occur (see supplementary material Sec. 1 for threshold settings).

The reflection is diffuse [see Fig. 1(b)] under the assumption of local thermal equilibrium. The probability density functions for the reflection speed ν and angle θ are derived from the Maxwell-Boltzmann distribution 42,43 and are given by

$$f(v) = 2\beta^2 v^3 e^{-\beta v^2},$$
 (2)

$$f(\theta) = \sin(2\theta), \quad \theta \in \left[0, \frac{\pi}{2}\right].$$
 (3)

Here, $\beta = m/(2k_BT)$, where m is the molecule mass, k_B is the Boltzmann constant, and T is the temperature. The reflection angle θ is defined as the polar angle between the reflected velocity vector and the surface normal, where $\theta \in [0, \pi/2]$ ensures physical validity (negative angles would correspond to unphysical penetration into the solid wall). The molecules adsorbed on the wall for a period of time, satisfying the exponential distribution⁴⁴

$$f(t) = \frac{\exp\left(-\frac{t}{t_{ad}}\right)}{t_{ad}}.$$
 (4)

Here, t_{ad} represents the average adsorption time. The feature is included to represent the physical processes of adsorption and condensation on regolith particles, ¹¹ particularly under low-temperature conditions.

B. Porous media computing domain

We first adopt periodic ball-and-stick structures for testing in Secs. II and III, as illustrated in Fig. 1(c). Such geometry corresponds to typical pore network models for sedimentary media. The structure consists of spherical pore-bodies connected by cylindrical pore-throats, with the centers of the pore-bodies located at the vertices of the cubes. Each periodic unit includes a pore-body surrounded by six half pore-throats. Geometric variables include: pore-body radius (R), pore-throat radius (r), and pore-throat length (L). The pore-throat length includes the spherical crown height at the two body-throat junctions. Additional geometric constructs are employed in Secs. II C and IV A for algorithm validation purposes.

Molecular trajectories scale with the structure, so we can simply adjust the medium geometry by varying the dimensionless pore-throat radius ($r^* = r/R$) and dimensionless pore-throat length ($L^* = L/R$). To prevent the overlap of pore-throats connected to the same pore-body, r^* must not exceed 0.707.

Previous studies show granular or sedimentary media are of pore-throat length-to-diameter ratio mostly ranging from 0.25 to 5, and of pore throat-to-body aspect ratio ranging from 0.6 to 0.7. 47,48 In this study, we vary these parameters in much larger ranges: pore-throat length-to-diameter ratio from 0.15 to 12, and pore throat-to-body aspect ratio from 0.1 to 0.7.

C. Determination of the diffusion coefficient

The diffusion coefficient, D_{sim} , is measured using the Einstein relation for self-diffusion 29,49

$$D_{sim} = \phi \langle (l(t))^2 \rangle / 6t, \tag{5}$$

where ϕ represents the porosity, and $\langle (l(t))^2 \rangle$ is the mean square displacement (MSD). The porosity is included to ensure that the data aligns with Fick's first law (see supplementary material Sec. 2). Since the molecular trajectories are velocity-invariant, the dimensionless diffusivity (D^*_{sim}) is calculated as

$$D_{sim}^* = D_{sim}/(R\overline{\nu}). \tag{6}$$

Here, $\overline{v} = \sqrt{8k_BT/\pi m}$ is the mean velocity of a gas molecule.

For each specific structure, 10 000 test molecules are simulated, and MSD data are collected at different times. As shown in Fig. 2(a), the MSD scales linearly with time, consistent with Eq. 5. The diffusion coefficient is computed by performing a linear fit of MSD vs time. Due to the inherent randomness in molecular trajectories, variations exist between the results from different simulations. To account for this, we divide the 10000 molecules into ten subgroups (each containing 1000 molecules) and perform independent linear fits to obtain separate diffusion coefficients. These subgroup coefficients serve as statistical samples of the theoretical diffusion coefficient and the overall diffusion coefficient of 10 000 molecules $(\overline{D_{sim}^*})$ is the mean of these subgroup values. Using a one-sample t-test,5 we evaluate whether this sample mean $(\overline{D_{sim}^*})$ agrees with the population mean (theoretical diffusion coefficient). The resulting 95% confidence intervals for the theoretical value are found to be an order of magnitude smaller than the sample mean, demonstrating robust statistical reliability of our simulations.

To validate the algorithm, we run a self-diffusion simulation in an infinitely long circular tube and calculate the diffusion coefficient. The dimensionless diffusion coefficient calculated for a tube with a dimensionless diameter of 3 (three times the characteristic length scale for normalization) is 1.01, while the theoretical value [Eq. (1)] is 1. We further verify the method by simulating straight tubes with square and elliptical cross sections, obtaining diffusion coefficients that consistently match their respective theoretical values⁵¹ (see supplementary material Sec. 3). These results collectively confirm the accuracy and robustness of our method.

D. Diffusion coefficient result

First, we investigate the relationship between the diffusion coefficient and geometrical parameters. As shown in Figs. 2(b) and 2(c), the dimensionless diffusion coefficient is plotted as a function of L^* for r^* values of 0.1 and 0.2, and as a function of r^* for an L^* value of 0.5, under conditions of no adsorption. The simulation reveals an intuitive relationship: the diffusion coefficient is negatively correlated with pore-throat length (L^*) and positively correlated with pore-throat radius (r^*) when another geometric parameter is held constant.

The adsorption effect reduces the self-diffusion rate. As shown in Fig. 2(d), for a structure with $L^*=0.41$ and $r^*=0.1$, the self-diffusion coefficient decreases as the average adsorption time $(t_{ad}^*=\bar{\nu}t_{ad}/R,$ characterizing the ratio between adsorption time and flying time) increases. When the average adsorption time is significantly larger than the flying time $(t_{ad}^*\gg 1)$, the self-diffusion coefficient is inversely proportional to the average adsorption time. This occurs because, for the same displacement, the time required is proportional to the number of collisions and, consequently, the number of adsorptions.

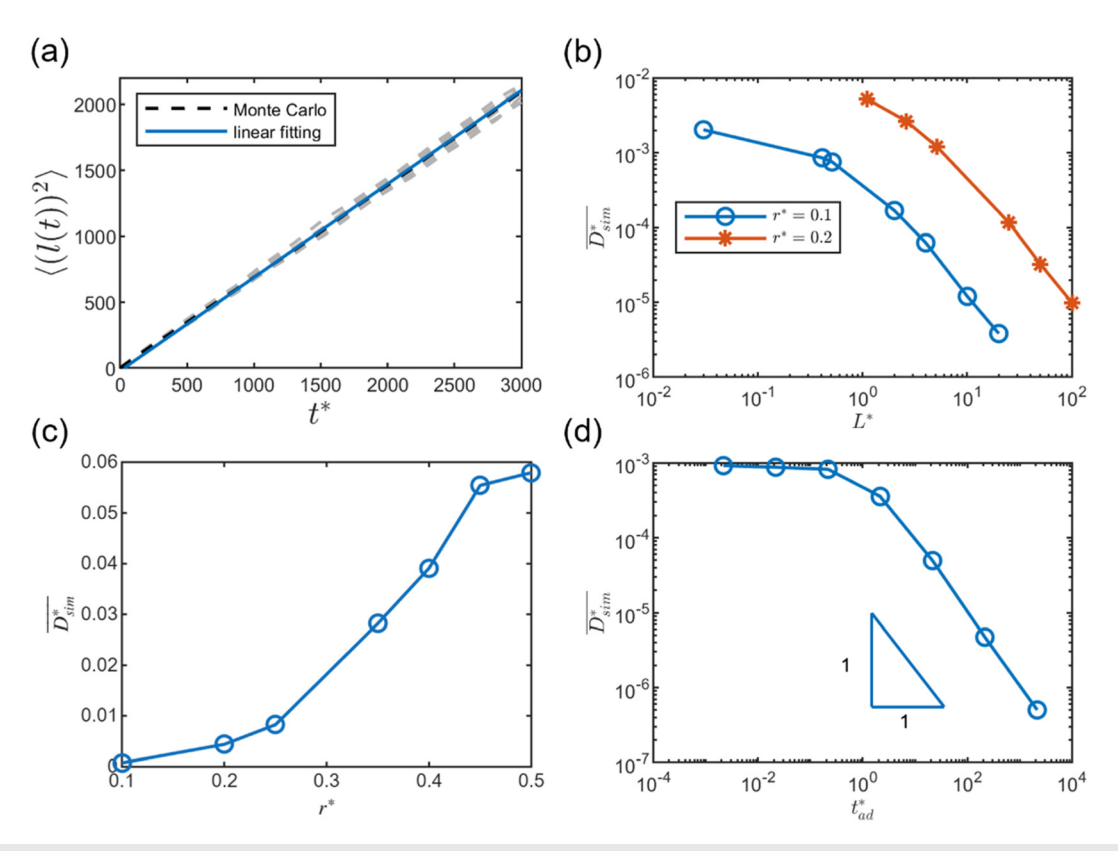


FIG. 2. (a) Mean squared displacement (MSD) vs time for: 10 000 molecules (black dashed), linear fit (blue solid), and ten subgroups of 1000 molecules (gray dashed). (b) Dimensionless diffusion coefficient as a function of L^* for $r^* = 0.1$ and 0.2, under conditions of no adsorption. (c) Dimensionless diffusion coefficient as a function of r^* for $L^* = 0.5$, under conditions of no adsorption time (t^*_{ad}), for $L^* = 0.41$ and $r^* = 0.1$. When t^*_{ad} exceeds 10, the diffusion coefficient is inversely proportional to t^*_{ad} .

We note that $t_{ad}^* \gg 1$ is very common on extraterrestrial surface regolith, as discussed in supplementary material Sec. 4.

III. PROBABILITY-BASED PORE NETWORK MODELING APPROACH

Although the TPMC method effectively simulates Knudsen diffusion in porous media, its computational cost becomes prohibitive at large spatial and temporal scales. Furthermore, the algorithm inherently introduces statistical fluctuations, necessitating extensive simulations to ensure accuracy and convergence.

To overcome these limitations, we develop a probability-based PNM approach that utilizes pore-scale information to enable simulations at larger scales. In this approach, we use the probability of the molecule being inside a particular geometric structure to represent the volatile spatial distribution, replacing the gas concentration, as the latter is excessively stochastic in low-density conditions.

A. Pore body-throat duality

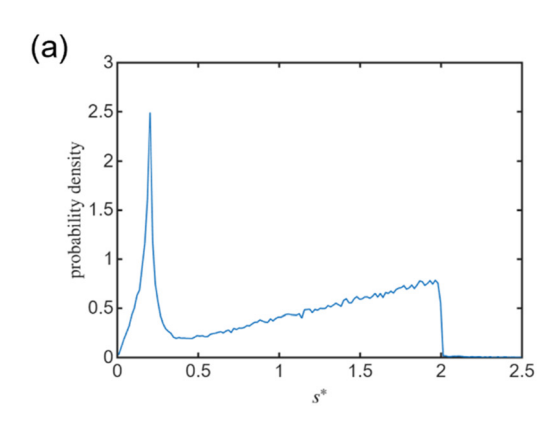
1. Duality of molecular trajectory properties

The motion of gas molecules during Knudsen diffusion is governed by the geometry of porous confinement. We analyze statistical properties of molecular trajectories obtained from TPMC

simulations to investigate the structural characteristics of porous media.

The molecular trajectory length distribution exhibits dual characteristics. As shown in Fig. 3(a), the distribution of the dimensionless molecular trajectory length ($s^* = s/R$, the length of the straight-line segments of molecular trajectories normalized by R) for a structure with $r^* = 0.1$ and $L^* = 2.01$ exhibits two peaks. These peaks correspond well to the diameters of the pore-body and pore-throat, respectively.

The residence time of molecules in a periodic unit [see Fig. 1(c)] also exhibits dual characteristics. As shown in Fig. 3(b), the distribution of the dimensionless residence time ($\tau^* = \bar{\nu}\tau/R$) within a periodic unit [see Fig. 1(c)] is calculated for a structure with $r^* = 0.5$ and L/2r = 0.47 and 10.27. The residence time represents the duration from when a molecule enters a unit until it leaves and moves to another unit. For systems with short pore-throats (L/2r = 0.47), where the structure is predominantly composed of pore-bodies, the logarithmic probability density is linear, corresponding to an exponential distribution. This characteristic demonstrates that the unit, i.e., the pore-body, exhibits the Markov property, meaning the probability of a molecule exiting a pore-body is independent of its residence time within it. In contrast, for systems with long pore-throats (L/2r = 10.27), where the structure is primarily comprised of pore-throats, the distribution curve transitions to a concave shape. This suggests



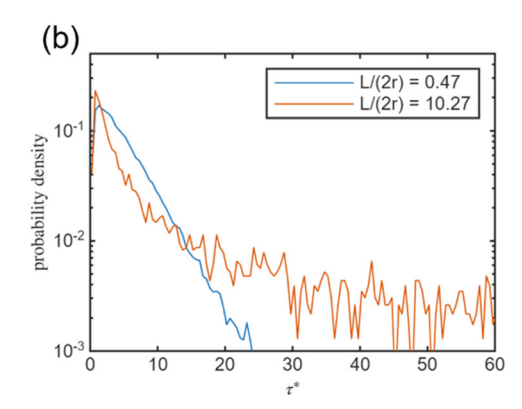


FIG. 3. (a) Distribution of dimensionless molecular trajectory length. Data are obtained from TPMC simulations with $r^* = 0.1$ and $L^* = 2.01$. (b) Distribution of the dimensionless residence time within a periodic unit. Data are obtained from TPMC simulations with $r^* = 0.5$ and pore-throat length-to-diameter ratios (L/2r) of 0.47 and 10.27.

that, unlike pore-bodies, a pore-throat does not obey the Markov property, which means that the probability of a molecule exiting the pore-throat is influenced by its residence time within it. In addition, for both distributions, the probability of very short residence times is low, as leaving a unit requires a finite amount of time.

2. Distinct diffusion behaviors in the pore-body and pore-throat

The molecular trajectory duality, especially in the Markov property applicability, implies the necessity to separately characterize the diffusion behaviors in the pore-body and pore-throat for upscaled modeling.

As shown in Fig. 4(a), we analyze the directions in which molecules exit a pore-body or pore-throat relative to their entry directions. To simplify statistical analysis and facilitate clear interpretation, all molecules are set to enter from the -x direction by rotating the coordinate system. Pore-bodies have six possible exit directions: -x, x, -y, y, -z, and z. Therefore, pore-throats have only two exit directions: -xand x. The statistical data are obtained from TPMC simulations with $r^* = 0.2$ and length-to-diameter ratios of 0.2 and 10.1. Figure 4(b) shows that the exit direction of molecules from a pore-body is uniformly distributed and independent of the entry direction. We classify structures exhibiting this property as Knudsen-isotropic, whereas those lacking it are termed Knudsen-anisotropic. However, for pore-throats, the exit direction depends on the length-to-diameter ratio [see Fig. 4(c)]. Molecules passing through shorter pore-throats are more likely to exit in the same direction as they entered (+x), while molecules passing through longer pore-throats are more likely to exit in the opposite direction (-x). We refer to these as the same-direction molecules and opposite-direction molecules, respectively. This phenomenon demonstrates that pore-throats act as Knudsen-anisotropic structures.

In summary, pore-bodies and pore-throats exhibit distinct properties in history-dependency and in Knudsen-isotropy:

 Pore-bodies satisfy the Markov property that the probability of a molecule exiting a pore-body is independent of its residence time within it; in contrast, pore-throats do not exhibit this property. (2) Pore-bodies are Knudsen-isotropic that the exit direction of molecules from a pore-body is uniformly distributed and independent of the entry direction; in contrast, pore-throats are Knudsen-anisotropic.

This distinction between pore-body and pore-throat allows us to consider the PNM method for upscaled modeling, which simplifies the complex void space of porous media into two basic structures: porebodies and pore-throats that connect them. We therefore develop a probability-based PNM algorithm to simulate Knudsen diffusion and obtain the upscaled diffusivity.

B. Algorithm

1. Probability-based PNM framework

As the physical context is a rarefied gas, interactions between gas molecules are negligible, and physical quantities exhibit significant fluctuations. As a result, pressure and concentration are unsuitable for representing the spatial distribution of the gas system. Instead, the p-PNM algorithm uses the probability of a molecule residing in a specific structure, i.e., pore-body or pore-throat, at a given time to represent the volatile spatial distribution. If the total number of molecules is known, the product of this probability and the total number yields the expected number of molecules in a structure at any time.

The mass transfer is expressed by the transfer probability of a molecule between two structures per unit time interval. The transfer probability is positively correlated with the time interval and inversely correlated with the distance between the two structures. We only consider the transfer probability between adjacent structures for simplicity as a first-order approximation. By calculating the transfer probabilities between all adjacent structures at each time step, the probabilities of molecules residing in all structures can be updated.

We denote the probability of the molecule residing in pore-body i and pore-throat j as p_i and p_j . Each pore-body is assigned a temperature T_i to represent the temperature distribution, and the temperature of the pore-throat is set as the average of the two adjacent pore-bodies. The average adsorption time of the molecules on the solid wall is denoted as t_{ad} .

As shown in Fig. 5, for each time step (Δt), the algorithm repeats the following four steps:

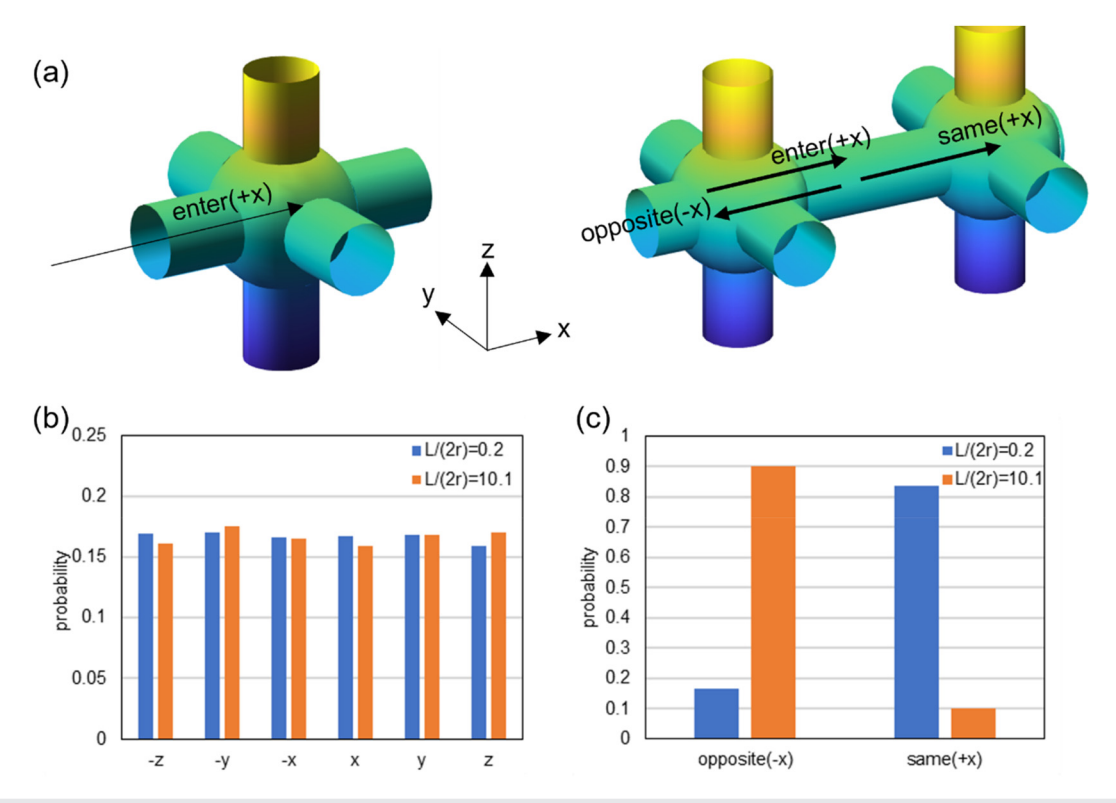


FIG. 4. (a) Diagram illustrating the setup for (b) and (c). The molecules are set to enter from the -x direction by rotating the coordinate system, and the exit directions are counted. (b) and (c) Probability of the exit directions of molecules in pore-bodies and pore-throats. Data are obtained from TPMC simulations with $r^* = 0.2$ and length-to-diameter ratios of 0.2 and 10.1.

(1) Calculate the transfer probability $L_{i \to j}^m$ from pore-body i to each connecting pore-throat j at the mth time step.

$$L_{i \to i}^m = p_i^m P_{p,i \to j},\tag{7}$$

where p_i^m is the probability of the molecule residing in porebody i at the m-th time step and $P_{p,i \to j}$ is the exit probability of a molecule in pore-body i within one time step Δt . Since the pore-body is Knudsen-isotropic, $P_{p,i \to j}$ depends only on the pore-throat radius. In addition, since the pore-body satisfies the Markov property, $P_{p,i \to j}$ is calculated by evaluating the cumulative distribution function (CDF) of the exponentially distributed pore-body residence time at the specified time Δt .

(2) Calculate the transfer probabilities of molecules in pore-throat j to the two adjacent pore-bodies i₁ and i₂ at the m-th time step. Since the pore-throat is Knudsen-anisotropic, molecules coming from the two adjacent pore-bodies (i.e., two directions) are counted separately, and the transfer probabilities to two adjacent pore-bodies are also calculated separately. In addition, since the pore-throat does not satisfy the Markov property, the exit probability is related to the residence time of molecules. Therefore, the transfer probabilities from the pore-throat to adjacent pore-bodies need to account for molecules with different residence times and motion directions (i.e., same-direction and opposite-direction) separately.

The transfer probabilities of molecules in pore-throat j to the two adjacent pore-bodies i_1 and i_2 at the m-th time step are given by

$$Q_{j \to i_1}^m = \sum_{k=0}^{K-1} L_{i_1 \to j}^{m-k} \left(F_o^{k+1} - F_o^k \right) (1 - P_{t,j}) + L_{i_2 \to j}^{m-k} \left(F_s^{k+1} - F_s^k \right) P_{t,j},$$
(8)

$$Q_{j \to i_2}^m = \sum_{k=0}^{K-1} L_{i_1 \to j}^{m-k} \Big(F_s^{k+1} - F_s^k \Big) P_{t,j} + L_{i_2 \to j}^{m-k} \Big(F_o^{k+1} - F_o^k \Big) (1 - P_{t,j}),$$
(9)

where $P_{t,j}$ represents the proportion of same-direction molecules in pore-throat j, k is the time step index, and F_o^k (or F_s^k) represents the probability that the residence time of the opposite-direction (or same-direction) molecules in pore-throat j is shorter than $k\Delta t$. To simplify the calculation, the residence time of molecules in the pore-throat is truncated to a maximum of K time steps. To ensure conservation, F_s^K and F_o^K are set to unity. For computational simplicity, the algorithm assumes that $P_{t,j}$ is independent of residence time. Although this assumption does not hold, it does not significantly impact the final result. (See supplementary material Sec. 5)

(3) Calculate the change in the probability of the molecule residing in pore-body *i* at the *m*-th time step.

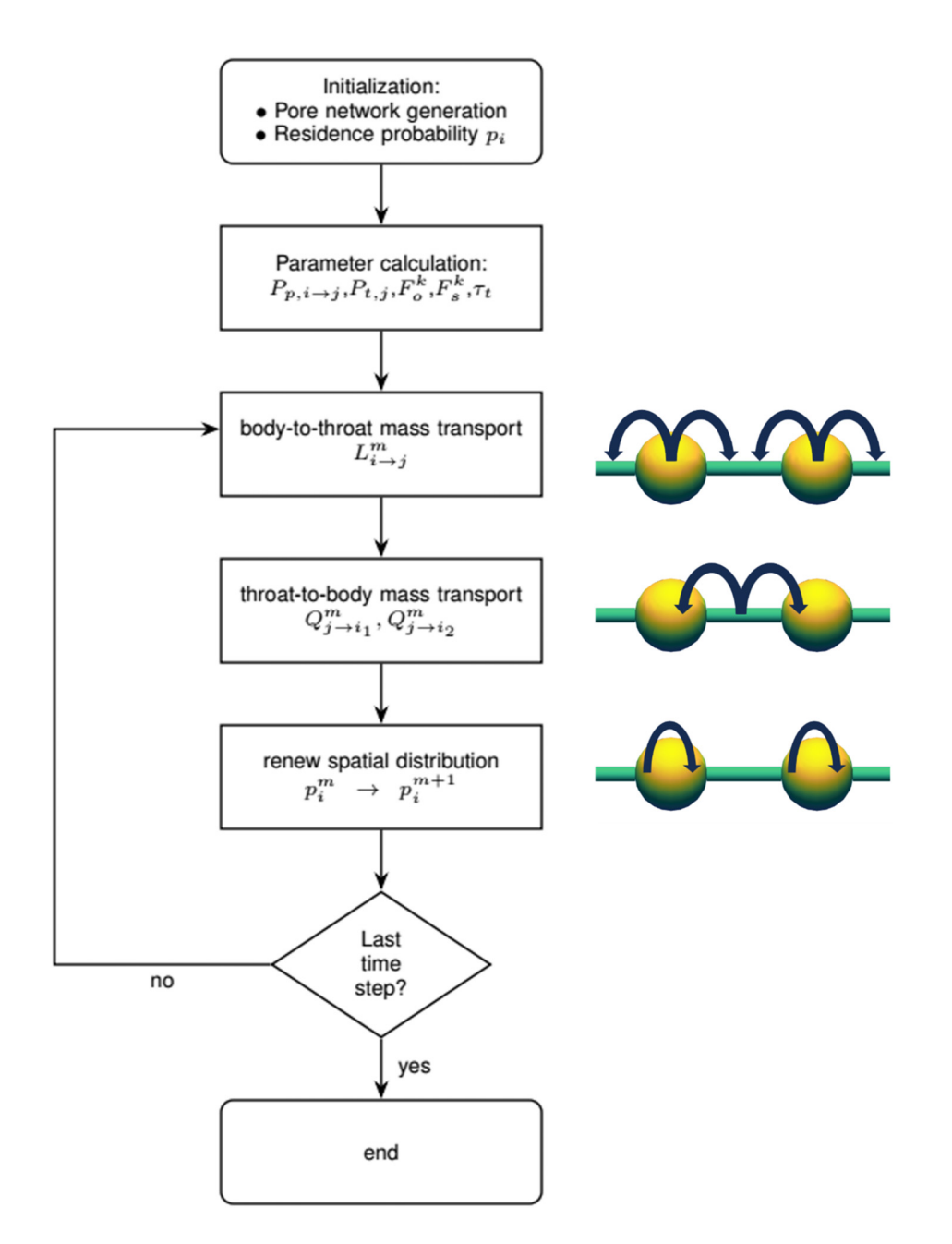


FIG. 5. P-PNM algorithm flow chart.

$$p_i^{m+1} = p_i^m - \sum_{j} (L_{i \to j}^m - Q_{j \to i}^m), \tag{10}$$

where j represents all pore-throats connected to pore-body i. In addition, the probability of the molecule residing in pore-throat j at mth time step is

$$p_j^m = \sum_{i=i_1,i_2} \sum_{k=0}^K L_i^{m-k} - Q_{j \to i}^{m-k}, \tag{11}$$

where this value is not actively used in the computational algorithm and can be determined through post-processing.

The parameters required for the algorithm include the exit probability $P_{p,i \to j}$, the proportion of same-direction molecules in the pore-throat $P_{t,j}$ and the probability that the residence time of the opposite-direction and same-direction molecules in the pore-throat is shorter than $k\Delta t$, i.e., F_o^k and F_s^k . These parameters are determined by the geometry, temperature, adsorption time, and other physical quantities.

In addition, we also need to determine two hyperparameters, K (maximum pore-throat residence time steps) and Δt (time step), to implement the numerical simulation. Once these parameters and hyperparameters are obtained, we can simulate Knudsen diffusion in

porous media with arbitrary pore-body and pore-throat structures, using this p-PNM method.

2. Key parameters in ball-stick structures

For demonstration, we derive the required parameters in the balland-stick structures as shown in Fig. 1(c). We denote the radius of pore-body i as R_i , while the length and radius of pore-throat j as L_j and r_b respectively. The calculation methods are as follows:

(1) The exit probability of a molecule in pore-body i to pore-throat j within one time step P_{p,i→j}. Given that the residence time of the molecule in the pore-body follows an exponential distribution, the exit probability for any time can be calculated based on the exit probability and average time of a single straight-line segment.

If a molecule is uniformly ejected from the inner surface of the pore-body via diffuse reflection (satisfying Eq. 3) and collides with the inner surface again, its average distance is $\pi R_i/2$. The interface between the pore-body and pore-throat is a spherical crown, and the probability of the molecule being ejected into the pore-throat is approximated as the ratio of the crown area to the sphere area: $p_{p0} = (1 - (1 - \sqrt{r_j/R_i}))/2$. That is, the probability of the molecule exiting the pore-body at time $t_0 = \pi R_i/2\overline{\nu} = \pi R_i/2\sqrt{8k_BT_i/\pi m}$ is p_{p0} .

Therefore, the exit probability of the molecule in the pore-body within one time step Δt is

$$P_{p,i\to j} = 1 - \exp[(\Delta t/t_0)\ln(1-p_{p0})].$$
 (12)

(2) The proportion of same-direction molecules in pore-throat j, P_{t,j}, and the probability that the residence time of the opposite-direction (or same-direction) molecules in pore-throat j is shorter than kΔt, F_o^k (or F_s^k). These parameters related to the pore-throat are obtained directly from TPMC simulations. It should be noted that the collected data depend only on the length-to-diameter ratio of the pore-throat, eliminating the need for separate simulations for structures with different pore-throat radii.

 $P_{t,j}$ is assumed to be a function of the pore-throat length-to-diameter ratio. Given that the proportion tends to 1 for very short pore-throats and 0 for very long pore-throats, the TPMC simulation data is fitted to the form $a/(a+(L_j/r_j)^b)$, yielding

$$P_{t,j} = \frac{2.118}{2.118 + \left(L_j/r_j\right)^{0.9079}}. (13)$$

 F_s^o and F_s^k are obtained by interpolating the CDFs of the residence distance for opposite-direction and same-direction molecules. The residence distance is the distance a molecule travels from entering to exiting a pore-throat. Due to scale independence, the CDF of the ratio of the residence distance to the pore-throat radius depends only on the pore-throat length-to-diameter ratio. The CDFs are denoted as $F_{\lambda,o}(\lambda; L_j/2r_j)$ and $F_{\lambda,s}(\lambda; L_j/2r_j)$, which are obtained from TPMC simulations. Both functions equal 0 for negative λ and 1 for sufficiently large positive λ . Using these CDFs, F_s^o and F_s^c are given by

$$F_o^k/F_s^k = F_{\lambda,o}/F_{\lambda,s} \Big(k\Delta t \sqrt{4k_B(T_{i1} + T_{i2})/\pi m}/r_j; L_j/2r_j \Big).$$
 (14)

In the computational implementation, the discrete data points of these CDFs are pre-stored in a file. During program execution, specific values are obtained through linear interpolation.

(3) The adsorption feature. If the adsorption time t_{ad} is not zero, the parameter calculation methods are modified as follows: The exit probability becomes

$$P_{p,i\to j} = 1 - \exp[(\Delta t/(t_0 + t_{ab}))\ln(1 - p_{p0})]. \tag{15}$$

The probability that the residence time of the opposite-direction and same-direction molecules in the pore-throat is shorter than $k\Delta t$ becomes

$$F_o^k/F_s^k = \sum_{n=0}^{5000} P_{No}/P_{Ns}(n) \times F_{\lambda,o}/F_{\lambda,s} \Big[(k\Delta t - nt_{ab}) \sqrt{4k_B(T_{i1} + T_{i2})/\pi m} \Big].$$
 (16)

where $P_{No}(n)$ and $P_{Ns}(n)$ are the probabilities of the number of collisions of the opposite-direction and same-direction molecules in the pore-throat, obtained from TPMC simulations. The number of collisions is truncated to a maximum of 5000 to ensure computational accuracy. These probabilities also depend only on the pore-throat length-to-diameter ratio.

3. Hyperparameter setup

As discussed above, two hyperparameters: K (maximum pore-throat residence time steps) and Δt (time step) need to be determined before simulation. We note that these are not empirical parameters for fitting, but are of very solid physical meaning and thus are subject to clear constraints.

First, if Δt is much larger than the residence time within a specific structure (pore-body or pore-throat), the approach of only considering the transfer probability between adjacent structures leads to significant errors; if it is too small, comparable to or shorter than the flight time of a molecule, the presumption of adopting probability would fail. Moreover, F_o^k and F_s^k are essentially samples of the CDFs, where K represents the number of sampling points and Δt is the sampling interval. The accuracy of the CDFs' representation directly impacts the precision of the p-PNM simulation. Therefore, a larger K is favored for accuracy, but increasing K also increases computational cost. Additionally, Δt must be carefully chosen: if it is too large, details of the CDFs may be lost; if it is too small, a larger K is required to maintain accuracy.

We set the hyperparameters by comparing the self-diffusion coefficients obtained from p-PNM (D_{pred}) and TPMC simulations ($\overline{D_{sim}}$) in the ball-and-stick structures as shown in Fig. 1(c) with uniform temperature. We evaluate the algorithm based on relative error ($D_{pred} - \overline{D_{sim}}$)/ $\overline{D_{sim}}$. The self-diffusion simulations are performed on a 51 × 51 × 51 PNM (51 pore-bodies in each x, y, and z direction). The coordinates of the central pore-body are set as the origin, and the initial condition is set as $p_i = 1$ for the central pore-body and 0 for all other pore-bodies. After simulating a period, the change in MSD over time is obtained, and the self-diffusion coefficient is derived from the slope of the linear fitting [Eq. (4)]. In addition, the MSD is calculated as the sum of the product of the probability of each pore-body and the square of its distance from the origin.

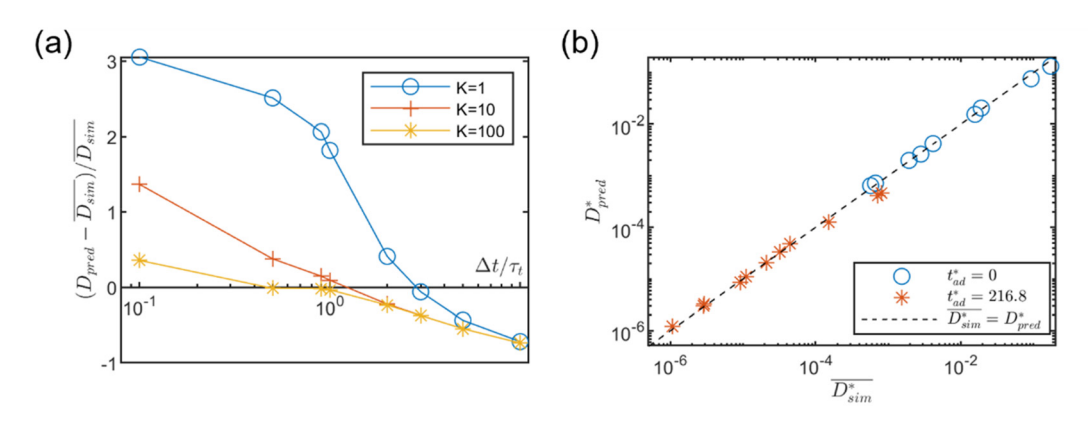


FIG. 6. (a) Relative error of the self-diffusion coefficient when the dimensionless pore-throat radius is 0.5 and the pore-throat length-to-diameter ratio is 10.27, predicted by the p-PNM algorithm as a function of the hyperparameters: the time step Δt (normalized by the characteristic residence time τ_t) and the maximum pore-throat residence time steps K. (b) Self-diffusion coefficients predicted by the p-PNM algorithm and TPMC results for various dimensionless pore-throat radii, pore-throat lengths, and average adsorption times.

The result of the relative error varying with the two hyperparameters is shown in Fig. 6(a). The relative error is minimized when Δt approaches the characteristic residence time in the pore-throat τ_b and the relative error decreases as the K increases. The characteristic residence time in the pore-throat τ_t is given by

$$\tau_{t} = \left(P_{t,j} F_{\lambda,s}^{-1}(0.5) + (1 - P_{t,j}) F_{\lambda,o}^{-1}(0.5) \right) / \overline{\nu}$$

$$+ t_{ad} \left[P_{t,j} \left(\sum_{n=0}^{5000} n P_{Ns}(n) \right) + (1 - P_{t,j}) \left(\sum_{n=0}^{5000} n P_{No}(n) \right) \right]. \quad (17)$$

Here, $F_{\lambda,o}^{-1}$ and $F_{\lambda,s}^{-1}$ represents the inverse functions of the CDFs, and $F_{\lambda,o}^{-1}(0.5)$ and $F_{\lambda,s}^{-1}(0.5)$ are the median residence distances of the opposite-direction and same-direction molecules, respectively.

To balance computational efficiency and accuracy, we adopt K = 20 and set the time step Δt to τ_t . In addition, when applying the p-PNM algorithm to media with a very wide pore size distribution, selecting an appropriate time step (Δt) becomes challenging.

C. Validation

The results for different dimensionless pore-throat radii, pore-throat length-to-diameter ratio, and average adsorption times are shown in Fig. 6(b). In most cases, the relative errors do not exceed 20% (See supplementary material Sec. 6). The p-PNM approach is thus capable of simulating the diffusion process of rarefied gas in porous media, provided the pore structure and other physical information are known.

IV. APPLICATIONS TO UPSCALING RAREFIED GAS DIFFUSION SIMULATION

In this section, we demonstrate p-PNM's capability to: (1) predict diffusion coefficients in sedimentary porous media, (2) model heterogeneous systems, and (3) simulate temperature-driven diffusion processes.

A. Calculation of the diffusion coefficient of sedimentary media

To validate the applicability of the p-PNM method to general porous media, we compared diffusion coefficients obtained from TPMC simulations with p-PNM predictions for three representative sedimentary structures (simple cubic (SC), face-centered cubic (FCC), and body-centered cubic (BCC) equal-diameter spherical packings) across varying average adsorption times. The pore structure is represented as an equivalent ball-and-stick model, from which the essential parameters for p-PNM implementation are derived. This representation enables the application of our p-PNM methodology for diffusion coefficient calculations.

Since the P-PNM method is sensitive to the pore structure, a suitable pore body-throat division method is required. The porous structures are transformed into equivalent ball-and-stick models using a two-step procedure. First, the Maximal Ball (MB) algorithm⁴ decomposes the pore space into maximal inscribed spheres (MISs) spheres that cannot be fully contained within any other inscribed sphere. This identifies pore-bodies as locally maximal MISs and porethroats as the constricted connections between them, with pore-throat radii defined by the smallest MIS in each connecting region. Second, we address the MB method's underestimation of porosity and characteristic pore sizes through geometric corrections: (1) pore-throat radii are redefined using the circumscribed circle radius at the tangent points between pore-body MISs and the solid matrix (adopting the smaller value when asymmetric pore body-throat connections occur), and (2) pore-body radii are systematically enlarged until the ball-andstick model's porosity converges with the measured bulk porosity of the original packing structure.

As shown in Fig. 7(a), the p-PNM predictions for SC, FCC, and BCC packings are mostly of error less than 40% compared to the TPMC-simulated values, across distinct normalized adsorption times ($t_{ad}^* = 0$, 2.17, 21.68, and 216.8), where $t_{ad}^* = \bar{v}t_{ad}/R_s$ and R_s is the sphere radius. Details of pore-body and pore-throat division are provided in the supplementary material Sec. 7.

B. Simulation in heterogeneous and irregular media

For heterogeneous and irregular systems, the TPMC algorithm becomes an impractical computational challenge in calculating the signed distance field. In contrast, the p-PNM algorithm readily accommodates such systems through direct assignment of geometric parameters to pore-bodies and pore-throats. In our implementation, we construct p-PNMs with fixed pore-throat radii ($r^* = 0.2$) and

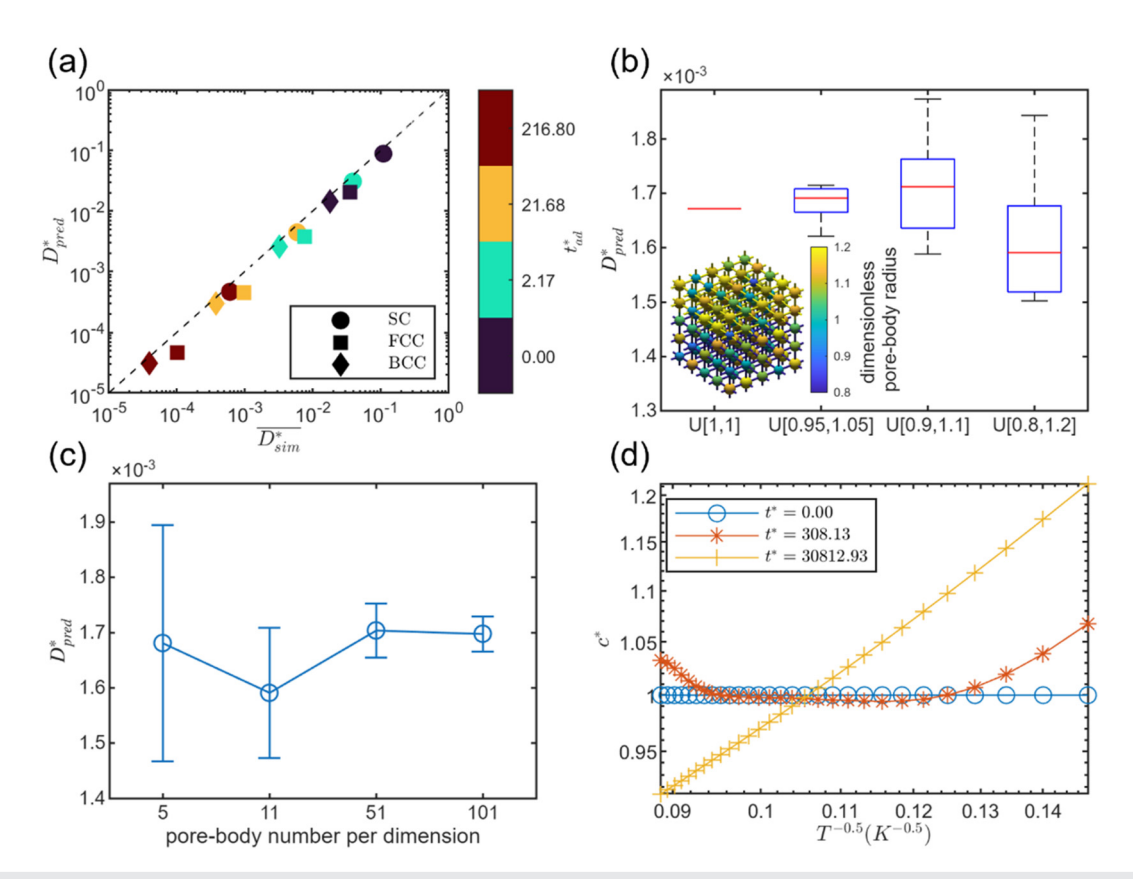


FIG. 7. (a) Dimensionless self-diffusion coefficients (normalized by R_s/\overline{v} , where R_s is sphere radius) predicted by the p-PNM algorithm and TPMC results for three sphere packings: simple cubic (SC), face-centered cubic (FCC), and body-centered cubic (BCC). Calculations are performed for average dimensionless adsorption times $t_{ad}^* = \overline{v}t_{ad}/R_s$ at values 0, 2.17, 21.68, and 216.8. (b) Diffusivity variations across different uniform pore-body radius distributions (with constant mean radius, which is used for normalization) for ten randomly generated 11 × 11 × 11 p-PNMs. These p-PNMs feature: (1) pore-body centers positioned on cubic lattice vertices (dimensionless side length of 4), and (2) fixed dimensionless pore-throat radii (r*=0.2). The subgraph is a schematic diagram of a heterogeneous PNM, with color representing the dimensionless pore-body radius. (c) Mean diffusion coefficient and the standard deviation as a function of p-PNM size (pore-body number per dimension). These p-PNMs feature: (1) pore-body centers positioned on a cubic lattice vertices (dimensionless side length of 4), (2) fixed dimensionless pore-throat radii (r*=0.2), and (3) dimensionless pore-body radius that is uniformly distributed between 0.8 and 1.2. (d) Temporal evolution of dimensionless number density (normalized by initial density) in the middle 29 units as a function of the pore-body temperature in a closed 31 × 1 × 1 PNM (r*=0.5, L*=2.27). The probability is inversely proportional to the square root of the temperature at the steady state.

constant pore-body center-to-center distances (arranged on cubic lattices with dimensionless side length = 4), while pore-body radii follow uniform distributions with varying ranges but constant expectation values (used for normalization), to simulate Knudsen diffusion under non-adsorbing, isothermal conditions. The distribution of dimensionless pore radii is divided into four cases: (1) all porebodies have the same radius; (2) the maximum dimensionless radius is 1.05 and the minimum is 0.95; (3) the maximum dimensionless radius is 1.1 and the minimum is 0.9; and (4) the maximum dimensionless radius is 1.2 and the minimum is 0.8. For each case, we generate 10 independent realizations of closed $11 \times 11 \times 11$ p-PNMs to compute the total diffusion coefficient. As shown in Fig. 7(b), the results demonstrate a clear trend where increased geometric heterogeneity correlates with broader distributions of the calculated diffusion coefficients. In addition, we also discussed the effects of heterogeneity in adsorption energy caused by differences in mineral composition in regolith, as shown in supplementary material Sec. 8.

We employed p-PNMs of varying dimensions to identify the REV. Specifically, p-PNMs of sizes $5 \times 5 \times 5$, $11 \times 11 \times 11$, $51 \times 51 \times 51$, and $101 \times 101 \times 101$ are generated following the aforementioned scheme, with the dimensionless pore-body radius ranging from 0.8 to 1.2. For each p-PNM size, we produced 10 random samples and conducted self-diffusion simulations to compute the diffusion coefficients. The mean diffusion coefficients and their standard deviations for each size are illustrated in Fig. 7(c). We define the REV as the smallest volume where the coefficient of variation (CV, defined as standard deviation/mean) remains below 5%.5 Based on our analysis, a p-PNM of at least $51 \times 51 \times 51$ satisfies this criterion (CV = 2.9%). In addition, Liu and Wang⁵⁴ demonstrate that the REV size for porosity is approximately 2.5 grain diameters, while the REV size for permeability varies from 15 to 25 grain diameters in both single-phase and two-phase flow systems. Considering the number of pore-bodies should be of the same order of magnitude as the number of grains, our results for the Knudsen condition are consistent with the conclusion.

C. Dynamic diffusion under temperature gradient

The TPMC method is computationally expensive for simulating long-term dynamic temperature-driven diffusion processes. In contrast, the p-PNM method offers an efficient alternative. A closed $31 \times 1 \times 1$ p-PNM is constructed, with different pore-bodies set at different temperatures but identical structures and initial number densities. The dimensionless pore-throat radius is 0.5, and the dimensionless pore-throat length is 2.27. As shown in Fig. 7(d), the number density (normalized by the initial number density) of the middle 29 units is plotted as a function of temperature and time. When the system reaches a steady state, the number density is found to be inversely proportional to the square root of the temperature. This shows that the p-PNM approach can effectively simulate the thermal transpiration under Knudsen conditions. This phenomenon occurs because the flux of an equilibrium rarefied gas is proportional to the product of the number density and the average velocity, and the average velocity is proportional to the square root of the temperature.

The p-PNM method enables the quantitative determination of volatile molecules' Soret coefficient (S_T), which characterizes thermodiffusion.⁵⁷ The Soret coefficient⁵⁸ is defined as

$$\nabla c = -cS_T \nabla T, \tag{18}$$

where T is temperature, and c is the molecular concentration of a steady zero current state. Our investigation employed the same p-PNM with an imposed linear temperature gradient of 0.01 K per pore-body superimposed on a base temperature field. The simulated Soret coefficients for water exhibit temperature dependence, decreasing from $5.94 \times 10^{-3} \ \text{K}^{-1}$ at $100 \ \text{K}$ to $2.35 \times 10^{-3} \ \text{K}^{-1}$ at $200 \ \text{K}$. In addition, the value varies with the geometric parameters.

V. LIMITATION OF THE p-PNM APPROACH

We note that this p-PNM method, although enabling faster simulation with acceptable accuracy, does have limitations due to the necessary simplifications:

- (1) This approach neglects molecule–molecule collisions and is only applicable to cases with extremely high Knudsen numbers, which need major modification if the Knudsen number is close to one.
- (2) This approach may not be suitable for scenarios with strong geometric or temperature heterogeneity, as it largely narrows down or even eliminates the appropriate domain to select hyperparameters.
- (3) This approach is only applicable to structures with clearly defined pore body-throat divisions and is not suitable for special media such as fibrous structures.
- (4) The model cannot characterize the effects of microporosity on the particle surface, which needs technical improvement in the future

VI. CONCLUSION

In this work, we investigate Knudsen diffusion in porous media with TPMC simulation and propose a probability-based PNM (p-PNM) method to model upscaled Knudsen diffusion in porous media, in order to study the volatile migration in the surface regolith of airless bodies. This p-PNM method greatly improves the calculation efficiency of Knudsen diffusion in porous media at the REV scale, and

obtains an error of less than 20% within typical structures. The key findings include:

- (1) Knudsen diffusion coefficient depends on both geometry and adsorption, which decreases with increasing structural obstruction (longer pore-throats and smaller pore-throat radii). The self-diffusion coefficient is inversely proportional to the average adsorption time when the adsorption time is much longer than the flying time.
- (2) We identify the pore body-throat duality for Knudsen diffusion in porous media. Pore-bodies exhibit Knudsen-isotropy (the exit direction of molecules in pore-bodies is uniformly distributed) and satisfy the Markov property (the exit probability of molecules in pore-bodies is independent of their residence time), while pore-throats are Knudsen-anisotropic and do not satisfy the Markov property.
- (3) We develop a p-PNM approach to model upscaled Knudsen diffusion behavior in porous media. Compared to TPMC, the p-PNM method requires significantly fewer computational resources and eliminates the stochastic noise inherent in TPMC, making it suitable for larger spatial and temporal scales. The method achieves an accuracy within 20% in predicting REV scale diffusion coefficients for typical structures.
- (4) Given the pore-body and pore-throat geometry and relevant physical parameters, the p-PNM method can: (1) predict diffusion coefficients in sedimentary porous media, (2) model heterogeneous systems, and (3) simulate temperature-driven diffusion processes.

This p-PNM approach can be applied for modeling volatile migration near the surface of airless bodies, to reveal near-surface redistribution, escape, and interplanetary propagation of volatile components in space, for geoscience and engineering purposes.

SUPPLEMENTARY MATERIAL

See the supplementary material for additional details for this article include the following eight sections:

Section 1: Collision Detection Threshold Configuration.

Section 2: Consistency of Self-Diffusion Coefficient is Consistent with the Fickian-type Diffusion Coefficient.

Section 3: Theoretical Diffusion Coefficient in Infinite Long Tubes.

Section 4: Estimation of Average Adsorption Time in Lunar Regolith (Soil).

Section 5: Residence Time Dependence of the Proportion of Same-direction Molecules.

Section 6: Predictive Accuracy of p-PNM for Homogeneous Balland-Stick Structures.

Section 7: The Pore-body and Pore-throat Divisions of Different Sedimentary Media.

Section 8: Effect of Adsorption Heterogeneity.

These sections provide further methodological details, datasets, and analyses referenced in the main text.

ACKNOWLEDGMENTS

This work was supported by the National Key Research and Development Program of China (No. 2021YFA0717200) and the National Natural Science Foundation of China (No. U23B6004).

AUTHOR DECLARATIONS

Conflict of Interest

The authors have no conflicts to disclose.

Author Contributions

Sunpeng Zhou: Conceptualization (equal); Formal analysis (lead); Investigation (lead); Methodology (lead); Validation (lead); Writing – original draft (lead); Writing – review & editing (equal). **Ke Xu:** Conceptualization (equal); Funding acquisition (lead); Investigation (supporting); Project administration (lead); Resources (lead); Supervision (lead); Writing – review & editing (equal).

DATA AVAILABILITY

The data that support the findings of this study are available within the article and its supplementary material.

REFERENCES

- ¹S. Li, P. G. Lucey, R. E. Milliken, P. O. Hayne, E. Fisher, J.-P. Williams, D. M. Hurley, and R. C. Elphic, "Direct evidence of surface exposed water ice in the lunar polar regions," Proc. Natl. Acad. Sci. U. S. A. 115(36), 8907–8912 (2018).
- ²Y. Jia, Z. Zhang, L. Qin, T. Ma, B. Lv, Z. Fu, C. Xue, and Y. Zou, "Research of Lunar Water-Ice and Exploration for China's Future Lunar Water-Ice Exploration," Space: Sci. Technol. 3, 0026 (2023).
- ³C. Ding, Q. Li, J. Xu, Z. Lei, J. Li, Y. Su, and S. Huang, "Moon-based ground penetrating radar derivation of the helium-3 reservoir in the regolith at the Chang'E-3 landing site," IEEE J. Sel. Top. Appl. Earth Obs. Remote Sens. 16, 2764–2776 (2023).
- ⁴V. Reshetnyk, Y. Skorov, M. Vasyuta, M. Bentley, L. Rezac, J. Agarwal, and J. Blum, "transport characteristics of the near-surface layer of the nucleus of Comet 67P/Churyumov–Gerasimenko," Sol. Syst. Res. 55(2), 106–123 (2021).
- ⁵E. G. Rivera-Valentin, D. G. Blackburn, and R. K. Ulrich, "Exploring the effects of overburden on the sublimation and transport of H₂O on Iapetus," Icarus 220(2), 808–820 (2012).
- ⁶Y. V. Skorov, R. V. Lieshout, J. Blum, and H. U. Keller, "Activity of comets: Gas transport in the near-surface porous layers of a cometary nucleus," Icarus 212(2), 867–876 (2011).
- ⁷J. Zhang, B. Zhou, Y. Lin, M.-H. Zhu, H. Song, Z. Dong, Y. Gao, K. Di, W. Yang, H. Lin, J. Yang, E. Liu, L. Wang, Y. Lin, C. Li, Z. Yue, Z. Yao, and Z. Ouyang, "Lunar regolith and substructure at Chang'E-4 landing site in South Pole–Aitken basin," Nat. Astron. 5(1), 25–30 (2020).
- ⁸G. H. Heiken, D. T. Vaniman, and B. M. French, *Lunar Sourcebook, a User's Guide to the Moon* (Cambridge University Press, Cambridge, UK, 1991).
- ⁹B. Hapke and H. Sato, "The porosity of the upper lunar regolith," Icarus 273, 75–83 (2016).
- ¹⁰Y. Li, Z. Wen, C. He, Y. Wei, and Q. Gao, "The mechanism for the barrier of Lunar regolith on the migration of water molecules," J. Geophys. Res. 128(3), e2022JE007254, https://doi.org/10.1029/2022JE007254 (2023).
- ¹¹B. Teolis, M. Sarantos, N. Schorghofer, B. Jones, C. Grava, A. Mura, P. Prem, B. Greenhagen, M. T. Capria, G. Cremonese, A. Lucchetti, and V. Galluzzi, "Surface exospheric interactions," Space Sci. Rev. 219(1), 4 (2023).
- ¹²L. Rubanenko, J. Venkatraman, and D. A. Paige, "Thick ice deposits in shallow simple craters on the Moon and Mercury," Nat. Geosci. 12(8), 597–601 (2019).
- ¹³A. R. Vasavada, D. A. Paige, and S. E. Wood, "Near-surface temperatures on mercury and the moon and the stability of polar ice deposits," <u>Icarus</u> 141(2), 179–193 (1999).
- ¹⁴N. Schorghofer and O. Aharonson, "The lunar thermal ice pump," Astrophys. J. 788(2), 169 (2014).
- ¹⁵H. A. Danque and K. M. Cannon, "Lunar polar volatile remobilization in regolith-filled craters," Icarus 411, 115953 (2024).
- ¹⁶W. Jitschin, in *Handbook of Vacuum Technology* (Wiley-VCH Verlag GmbH & Co. KGaA, Weinheim, Germany, 2016), pp. 83–166.

- ¹⁷D. A. Paige, M. A. Siegler, J. A. Zhang, P. O. Hayne, E. J. Foote, K. A. Bennett, A. R. Vasavada, B. T. Greenhagen, J. T. Schofield, D. J. McCleese, M. C. Foote, E. DeJong, B. G. Bills, W. Hartford, B. C. Murray, C. C. Allen, K. Snook, L. A. Soderblom, S. Calcutt, F. W. Taylor, N. E. Bowles, J. L. Bandfield, R. Elphic, R. Ghent, T. D. Glotch, M. B. Wyatt, and P. G. Lucey, "Diviner Lunar radiometer observations of cold traps in the Moon's South Polar Region," Science 330(6003), 479–482 (2010).
- ¹⁸D. A. Paige, M. C. Foote, B. T. Greenhagen, J. T. Schofield, S. Calcutt, A. R. Vasavada, D. J. Preston, F. W. Taylor, C. C. Allen, K. J. Snook, B. M. Jakosky, B. C. Murray, L. A. Soderblom, B. Jau, S. Loring, J. Bulharowski, N. E. Bowles, I. R. Thomas, M. T. Sullivan, C. Avis, E. M. De Jong, W. Hartford, and D. J. McCleese, "The Lunar reconnaissance orbiter diviner lunar radiometer experiment," Space Sci. Rev. 150(1), 125–160 (2010).
- ¹⁹C. Li, H. Hu, M.-F. Yang, Z.-Y. Pei, Q. Zhou, X. Ren, B. Liu, D. Liu, X. Zeng, G. Zhang, H. Zhang, J. Liu, Q. Wang, X. Deng, C. Xiao, Y. Yao, D. Xue, W. Zuo, Y. Su, W. Wen, and Z. Ouyang, "Characteristics of the lunar samples returned by the Chang'E-5 mission," Natl. Sci. Rev. 9(2), nwab188 (2022).
- ²⁰M. C. Bravo, "Effect of transition from slip to free molecular flow on gas transport in porous media," J. Appl. Phys. 102(7), 074905 (2007).
- ²¹N. Dongari and A. Agrawal, "Modeling of Navier-Stokes equations for high Knudsen number gas flows," Int. J. Heat Mass Transfer 55(15), 4352-4358 (2012)
- ²²J. Liu and J. Wei, "Knudsen diffusion in channels and networks," Chem. Eng. Sci. 111, 1–14 (2014).
- ²³W. Song, J. Yao, Y. Li, H. Sun, L. Zhang, Y. Yang, J. Zhao, and H. Sui, "Apparent gas permeability in an organic-rich shale reservoir," Fuel 181, 973–984 (2016).
- ²⁴X.-J. Zhang, in *Encyclopedia of Tribology*, edited by Q. J. Wang and Y.-W. Chung (Springer US, Boston, MA, 2013), pp. 3945–3947.
- ²⁵W. Steckelmacher, "Knudsen flow 75 years on: The current state of the art for flow of rarefied gases in tubes and systems," Rep. Prog. Phys. 49(10), 1083–1107 (1986).
- ²⁶J. M. Zalc, S. C. Reyes, and E. Iglesia, "The effects of diffusion mechanism and void structure on transport rates and tortuosity factors in complex porous structures," Chem. Eng. Sci. 59(14), 2947–2960 (2004).
- 27G. Steiner, "Two considerations concerning the free molecular flow of gases in porous ices," Astron. Astrophys. 240, 533–536 (1990); available at https://adsabs.harvard.edu/full/1990A%26A...240..533S.
- ²⁸L. Shen and Z. Chen, "Critical review of the impact of tortuosity on diffusion," Chem. Eng. Sci. 62(14), 3748–3755 (2007).
- ²⁹J. Fu, H. R. Thomas, and C. Li, "Tortuosity of porous media: Image analysis and physical simulation," Earth. Sci. Rev. 212, 103439 (2021).
- 30 L. Holzer, P. Marmet, M. Fingerle, A. Wiegmann, M. Neumann, and V. Schmidt, Tortuosity and Microstructure Effects in Porous Media: Classical Theories, Empirical Data and Modern Methods, edited by L. Holzer, P. Marmet, M. Fingerle, A. Wiegmann, M. Neumann, and V. Schmidt (Springer International Publishing, Cham, 2023), pp. 7–50.
- ³¹S. Russ, "Exact calculation of the tortuosity in disordered linear pores in the Knudsen regime," Phys. Rev. E 80(6), 061133 (2009).
- ³²P. Levitz, "Knudsen diffusion and excitation transfer in random porous media," J. Phys. Chem. 97(15), 3813–3818 (1993).
- ³³P. N. Henrion, "Knudsen diffusion in powders. Part I Critical examination of a gas diffusion relationship used in Knudsen flow permeametry," Powder Technol. 16(2), 159–166 (1977).
- ³⁴W. Macher, Y. Skorov, G. Kargl, S. Laddha, and S. Zivithal, "Transmission probability of gas molecules through porous layers at Knudsen diffusion," J. Eng. Math. 144(1), 2 (2024).
- 35D. H. Davis, "Monte Carlo calculation of molecular flow rates through a cylindrical elbow and pipes of other shapes," J. Appl. Phys. 31(7), 1169–1176 (1960).
- 36X. Jin, F. Huang, X. Cheng, Q. Wang, and B. Wang, "Monte Carlo simulation for aerodynamic coefficients of satellites in Low-Earth Orbit," Acta Astronaut. 160, 222–229 (2019).
- ³⁷R. Kersevan and M. Ady, "Recent developments of Monte-Carlo codes Molflow+ and Synrad+," in 10th International Particle Accelerator Conference (JACoW Publishing, 2019), Vol. 6.

- ³⁸M. M. Tomadakis and S. V. Sotirchos, "Ordinary and transition regime diffusion in random fiber structures," AlChe. J. 39(3), 397–412 (1993).
- 39S. Osher and R. Fedkiw, in *Level Set Methods and Dynamic Implicit Surfaces*, edited by S. Osher and R. Fedkiw (Springer New York, New York, NY, 2003), pp. 17–22.
- pp. 17–22.
 J.-M. Tucny, S. Leclaire, D. Vidal, and F. Bertrand, "Computation of Effective Viscosities for Rarefied Gas Flows Using Ray-Tracing," Int. J. Appl. Comput. Math. 9(5), 110 (2023).
- ⁴¹K. Meyerhoff and D. Hesse, "Determination of effective macropore diffusion coefficients by digital image processing," Chem. Eng. Technol. 20(4), 230–239 (1997).
- ⁴²C. J. H. Knox and L. F. Phillips, "Maxwell versus non-Maxwell velocity distributions for molecules emitted from a liquid surface," J. Phys. Chem. B 102(51), 10515–10520 (1998).
- ⁴³J. Greenwood, "The correct and incorrect generation of a cosine distribution of scattered particles for Monte-Carlo modelling of vacuum systems," Vacuum 67(2), 217–222 (2002).
- ⁴⁴D. Hlushkou, F. Gritti, A. Daneyko, G. Guiochon, and U. Tallarek, "How microscopic characteristics of the adsorption kinetics impact macroscale transport in chromatographic beds," J. Phys. Chem. C 117(44), 22974–22985 (2013).
- ⁴⁵H. Dong and M. J. Blunt, "Pore-network extraction from micro-computerized-tomography images," Phys. Rev. E 80(3), 036307 (2009).
- ⁴⁶R. Y. Yang, R. P. Zou, A. B. Yu, and S. K. Choi, "Pore structure of the packing of fine particles," J. Colloid Interface Sci. 299(2), 719–725 (2006).
- ⁴⁷R. I. Al-Raoush and C. S. Willson, "A pore-scale investigation of a multiphase porous media system," J. Contam. Hydrol. 77(1), 67–89 (2005).

- ⁴⁸H. Yang and M. T. Balhoff, "Pore-network modeling of particle retention in porous media," AlChE. J. 63(7), 3118–3131 (2017).
- ⁴⁹D. T. Gillespie and E. Seitaridou, in *Simple Brownian Diffusion: An Introduction to the Standard Theoretical Models*, edited by D. T. Gillespie and E. Seitaridou (Oxford University Press, 2012).
- ⁵⁰R. E. Walpole and R. H. Myers, Probability and Statistics for Engineers and Scientists (Prentice Hall, 2009).
- ⁵¹W. Steckelmacher, "The effect of cross-sectional shape on the molecular flow in long tubes," Vacuum 28(6), 269–275 (1978).
- ⁵²D. Silin and T. Patzek, "Pore space morphology analysis using maximal inscribed spheres," Physica A 371(2), 336–360 (2006).
- 53D. Zhang, R. Zhang, S. Chen, and W. E. Soll, "Pore scale study of flow in porous media: Scale dependency, REV, and statistical REV," Geophys. Res. Lett. 27(8), 1195–1198, https://doi.org/10.1029/1999GL011101 (2000).
- 54T. Liu and M. Wang, "Critical REV size of multiphase flow in porous media for upscaling by pore-scale modeling," Transp. Porous Media 144(1), 111-132 (2022).
- 55S. K. Loyalka, "Thermal transpiration in a cylindrical tube," Phys. Fluids 12, 2301–2305 (1969).
- 56C. C. Chen, I. K. Chen, T. P. Liu, and Y. Sone, "Thermal transpiration for the linearized Boltzmann equation," Commun. Pure Appl. Math. 60, 147-163 (2007).
- ⁵⁷S. Duhr and D. Braun, "Why molecules move along a temperature gradient," Proc. Natl. Acad. Sci. U. S. A. **103**(52), 19678–19682 (2006).
- ⁵⁸D. Zhao, A. Würger, and X. Crispin, "Ionic thermoelectric materials and devices," J. Energy Chem. 61, 88–103 (2021).